

Mitigation of Space-Charge Driven Fourth-Order Resonance by Beam Spinning

Yoo-Lim Cheon, Seok-Ho Moon, and Moses Chung*

Department of Physics, Ulsan National Institute of Science and Technology, Ulsan 44919, Republic of Korea

Dong-O Jeon*

Institute for Basic Science, Daejeon 34047, Republic of Korea

Recently discovered $4\sigma = 360^\circ$ fourth-order particle resonance sets one of the fundamental operational limits for high-intensity linear accelerators. To mitigate this nonlinear space-charge driven resonance and subsequent envelope instabilities, we propose a novel approach of using spinning beams with finite average canonical angular momentum. From the analytical and numerical simulation studies, we found that the spinning beams have an intrinsic characteristic that can suppress the impact of the fourth-order resonance on emittance growth and associated envelope instability. We use initially well-matched Gaussian beams in a periodic solenoidal lattice, and consider stripping of H^- (or D^-) beams by a thin foil inside a pair of solenoids placed before the main linac to inject the spinning beams.

One of the major issues in high-intensity linear accelerators (linacs) is to minimize halo formation and beam losses driven by strong space-charge forces [1–4]. An effective countermeasure against such effects could facilitate the applications of intense proton and ion beams to intensity-frontier particle and nuclear physics experiments, fusion materials irradiation test, nuclear waste transmutation, and accelerator-driven subcritical reactors. Through a detailed investigation on space-charge beam dynamics, several halo formation mechanisms have been identified, which include coherent instabilities (also called parametric resonances) [5–9] and incoherent resonances (also called particle resonances) [10, 11].

Recently, Jeon and coworkers [12] reported $4\sigma = 360^\circ$ (or 4:1) fourth-order particle resonance in high-intensity linacs for the first time and then verified it experimentally [13, 14]. Here, σ is the depressed phase advance per cell. Subsequent studies discovered that the fourth-order particle resonance is manifested predominantly over the envelope instability when σ is kept constant along the linacs [15–17]. In particular, Ref. 17 summarizes the difference between coherent instabilities and particle resonances. Further studies in Ref. 18 established that the general stop band for the $4\sigma = 360^\circ$ fourth-order particle resonance is $\sigma_0 > 90^\circ$ and $\sigma < 90^\circ$, where σ_0 is the zero-current phase advance. It is worth noting that the fourth-order resonance stop band is wider than the envelope instability stop band, and the envelope instability is induced following the fourth-order resonance only within the envelope instability stop band in the tune-depression space.

Certainly, it is desirable to overcome these operational limitations associated with space-charge driven resonances and instabilities. It has already been discussed (mainly in the context of high-intensity rings) that active suppression of coherent instabilities can be achieved through Landau damping [19] or nonlinear decoherence [20] using octupoles, feedback dampers, electron lenses, or dedicated nonlinear lattices to provide favorable tune spreads of beam particles. These methods are aiming for mitigating coherent instabilities originated from collective perturbations or envelope mismatches.

However, in high-intensity linacs, even for initially well-matched beams without any external repetitive perturbations, nonlinear space-charge forces can excite higher-order particle resonances. In particular, the fourth-order resonance stop band sets the fundamental operational limits.

Hence, in this Letter, we present a novel method of mitigating $4\sigma = 360^\circ$ fourth-order particle resonance in linacs by introducing the concept of beam spinning. The spinning beam has a non-zero average canonical angular momentum and exhibits a rigid-rotor rotation around the beam propagation axis. This scheme is based on two notable achievements in beam physics: i) a rigid-rotor beam equilibrium was obtained for an intense beam propagating through a periodic solenoidal lattice [21], and ii) a rotating beam was generated by stripping an ion beam inside a solenoid [22]. To take advantage of the beam spinning effect, we consider an axisymmetric system, where the canonical angular momentum is conserved. We note that many modern low-energy superconducting linacs adopt solenoid focusing and maintain the beam axisymmetric. For beam generation, we propose stripping of H^- (or D^-) beams by a foil inside a pair of solenoids installed in the medium energy beam transport (MEBT) line, and injecting the resultant spinning H^+ (or D^+) beams into the main linacs after proper matching.

We observe that the stop band and growth rate of coherent (or envelope) instability following the $4\sigma = 360^\circ$ fourth-order particle resonance are reduced for the spinning beams, because the beam mismatch triggered by the fourth-order resonance becomes smaller. We present both analytical and multi-particle simulation results to support this argument. In our analysis, non-KV Gaussian beams are initially rms-matched to a periodic solenoid focusing channel.

First, we make Poincaré-section plots to observe single particle trajectories for the $4\sigma = 360^\circ$ fourth-order resonance in the context of the particle-core model [23–25]. The evolution of the axisymmetric ($\partial/\partial\theta = 0$) transverse beam size r_b with canonical angular momentum is given

by the following envelope equation [21],

$$\frac{d^2 r_b(s)}{ds^2} + \kappa_z(s)r_b(s) - \frac{K}{r_b(s)} - \frac{\epsilon_T^2}{r_b^3(s)} = 0, \quad (1)$$

where $\kappa_z(s)$ is the lattice coefficient as a function of the axial coordinate s , and ϵ_T indicates the rms edge emittance which is four times the transverse rms emittance, $\epsilon_{\text{rms}} = \epsilon_T/4 = \sqrt{\epsilon_{\text{th}}^2 + \langle \hat{P}_\theta \rangle^2}/4$. Here, ϵ_{rms} is composed of thermal emittance $\epsilon_{\text{th}} = \sqrt{\det(\Sigma)}$, which is related to the determinant of 4×4 beam matrix Σ , and normalized average canonical angular momentum $\langle \hat{P}_\theta \rangle$, which represents the statistical average of $\hat{P}_\theta = \frac{P_\theta}{\gamma\beta mc}$ over the beam distribution [26, 27]. The space-charge perveance is defined by $K = q\lambda/2\pi\epsilon_0\gamma^3\beta^2 mc^2$ (in MKS units) with line charge density λ , where ϵ_0 is the vacuum permittivity, and m and q are the particle rest mass and charge, respectively. Here, c is the speed of light *in vacuo* and $\gamma = (1 - \beta^2)^{-1/2}$ is the relativistic mass factor. Even when the beam has non-zero canonical angular momentum, the matched solution for the envelope radius from Eq. (1) can be easily determined.

The equation of motion for radial particle coordinate r with Gaussian self-field obtained using Eq. (1) can be simplified as [2, 18]

$$r''(s) + \kappa_z(s)r(s) - \frac{\hat{P}_\theta^2}{r^3(s)} - K \frac{1 - e^{-[r^2(s)/\sigma_r^2(s)]}}{r(s)} = 0, \quad (2)$$

where $\sigma_r(s) = r_b(s)/\sqrt{2}$ is the rms beam radius. Here, the prime denotes the derivative with respect to s . The third term of Eq. (2) adds a nonlinear repulsive effect when the canonical angular momentum is not zero, and has the ability to change space-charge driven resonance structures. In this case, the particle never crosses the axis ($r = 0$) [2]. We note that $\hat{P}_\theta = r^2\theta' + (qA_\theta r/\gamma\beta mc)$ of a single particle is determined using the initial conditions, where the azimuthal vector potential is $A_\theta = B_z(s)r/2$ to leading order.

Under the solenoid magnetic field B_z , the equations of motion of a single particle are coupled in x - and y -directions of a laboratory frame. To remove the $x - y$ coupling, one normally performs a transformation from a laboratory to Larmor frame [1, 2]. The equation of motion of a single particle in the Larmor frame (X, Y) is then represented as

$$X_\perp''(s) + \kappa_z(s)X_\perp(s) - K \frac{1 - e^{-[r^2(s)/\sigma_r^2(s)]}}{r^2(s)} X_\perp(s) = 0, \quad (3)$$

where $X_\perp = X$ or Y , and $r^2 = X^2 + Y^2$. The canonical angular momentum is invariant under Larmor transformation and is expressed using $\hat{P}_\theta = XY' - YX'$. If \hat{P}_θ has a finite value, the nonlinear Gaussian self-fields provide an additional coupling between X and Y directions due to the r^2 components in the last term of Eq. (3). For the particle-core model, we assumed that every single particle has the same initial canonical angular momentum,

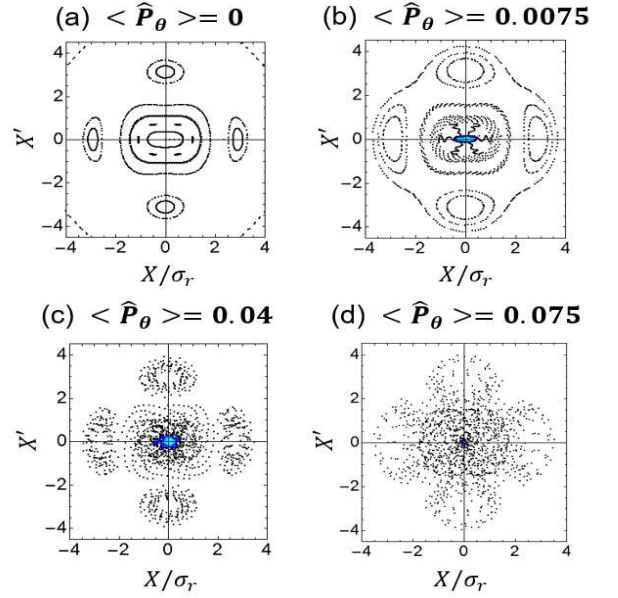


FIG. 1. Poincaré-section plots in the Larmor frame when $\sigma_0 = 100^\circ$ and $\sigma = 72^\circ$. (a) $\langle \hat{P}_\theta \rangle = 0$ (b) $\langle \hat{P}_\theta \rangle = 0.0075$ (c) $\langle \hat{P}_\theta \rangle = 0.0375$ (d) $\langle \hat{P}_\theta \rangle = 0.075$. It is worth noting that the coupling effect increases and resonance island structures become blurred as $\langle \hat{P}_\theta \rangle$ (in arbitrary units) increases.

such that $\langle \hat{P}_\theta \rangle = \hat{P}_\theta$, and $\langle \hat{P}_\theta \rangle$ remains constant along the lattice periods as well as the rms emittance.

Figure 1 shows the Poincaré-section plots in Larmor frame with various values of the canonical angular momentum when $\sigma_0 = 100^\circ$ and $\sigma = 72^\circ$. Here, the same periodic solenoidal lattice $\kappa_z(s) = \kappa_z(s + S)$ as in Ref. 18 is employed. We note that σ is calculated by $\sigma \equiv \epsilon_{\text{rms}} \int_0^S \frac{2}{\sigma_r^2(s)} ds$, where S is the lattice period. Hence, hereafter, σ represents the phase advance of an entire beam distribution, not of a single particle. If $\langle \hat{P}_\theta \rangle$ equals to zero as in Fig. 1(a), particles in X and Y directions have no coupling, showing that the four resonance islands are evidently separated from the central region with tune of 0.25 ($= 90^\circ/360^\circ$). On the other hand, in the cases of non-zero $\langle \hat{P}_\theta \rangle$ beams plotted in Figs. 1(b)–(d), coupling effect increases and the resonance islands become blurred. The separatrix and the central elliptical orbits merge, which indicates that the resonance particles trapped in the four separate islands enter the stable region and suppress the evolution of halo particles.

Supported by the analytical interpretation, we perform numerical simulations that will give clearer evidence for the mitigation phenomena of the $4\sigma = 360^\circ$ fourth-order particle resonance and the induced envelope instability. Hereon, we use the TraceWin particle-in-cell code [28]. The initial thermal emittance is $\epsilon_{\text{th}} = 6.85$ mm-mrad, and for non-spinning beams, it is equal to the rms emittance. The longitudinal rms emittance and phase advance are assumed to be very small so that the coupling between transverse and longitudinal dimen-

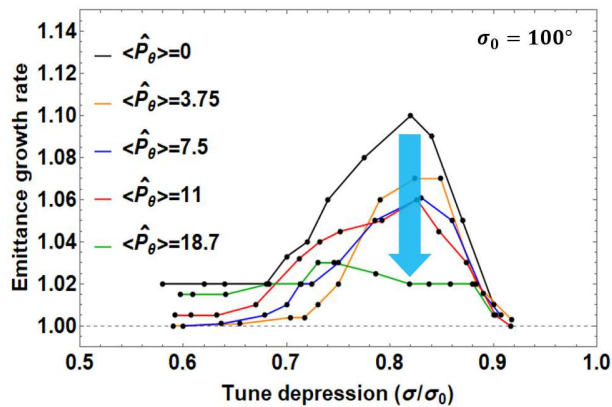


FIG. 2. Emittance growth rates during 50 lattice periods for $\sigma_0 = 100^\circ$ in which the $4\sigma = 360^\circ$ fourth-order particle resonance is dominant. Here, the unit of $\langle \hat{P}_\theta \rangle$ is mm-mrad. For non-zero $\langle \hat{P}_\theta \rangle$ beams, the emittance growth rates become smaller and flat over the tune depression space.

sions can be ignored. To generate spinning beams in the simulations, we load initial particles at the center of a solenoid field B_z without any average rotation. The total canonical angular momentum is then given by $P_\theta = qB_z(s=0)r^2/2$. Along the length of the solenoid, the magnetic field strength decreases, whereas the total canonical angular momentum is conserved. Outside the magnetic field region, where B_z vanishes, beam particles instead gain the mechanical angular momentum $P_\theta = \gamma\beta mcr^2\theta'$ due to the torque exerted from the fringe field at the exit of the solenoid [2, 29]. We propagate this spinning beam through the periodic solenoid focusing channel with initially well-matched conditions. The average initial canonical angular momentum is calculated over 100,000 particles. If we assume θ' to be the same for all particles, the rotating angle per lattice period would be approximately 30° , 45° , 60° , and 90° for $\langle \hat{P}_\theta \rangle = 3.75$, 7.5, 11, and 18.7 mm-mrad, respectively.

Figure 2 compares the emittance growth rates $\equiv (\epsilon_{\text{rms}} + \Delta\epsilon_{\text{rms}})/\epsilon_{\text{rms}}$ during 50 lattice periods for different values of canonical angular momentum. Over such a short propagation, the $4\sigma = 360^\circ$ fourth-order particle resonance is dominantly manifested against the envelope instability, i.e., the emittance growth is only affected by the fourth-order resonance under well-matched conditions. As discussed in Ref. 18, the fourth-order resonance stop band for $\sigma_0 = 100^\circ$ is $\sigma/\sigma_0 \leq 0.9$. Interestingly, as $\langle \hat{P}_\theta \rangle$ increases, the emittance growth rates become smaller and flat over the tune depression space. This implies that the emittance growth reaches a certain limit due to the mitigation of the fourth-order resonance because of the nonlinear coupling inherent to the spinning beams (see also Fig. 1).

Figure 3 shows the emittance growth rates over 200 periods for Gaussian beams as well as the envelope instability stop band of the equivalent KV beam. In this case, the beams propagate sufficiently long to induce envelope

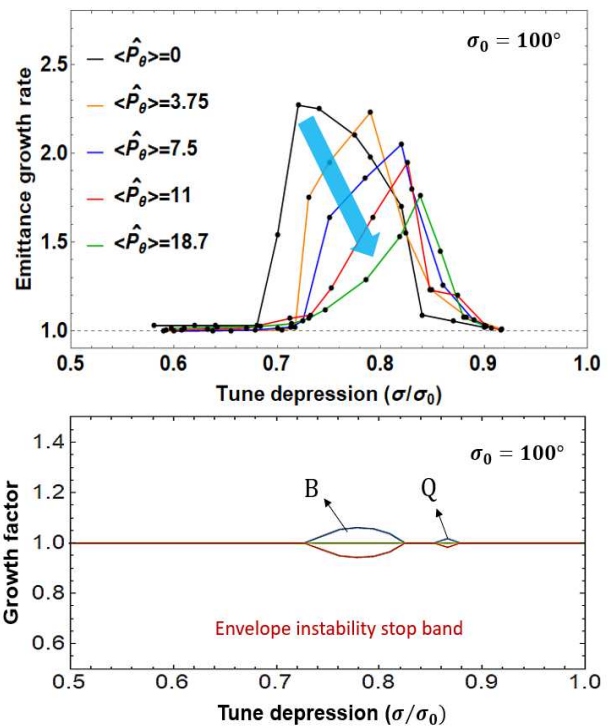


FIG. 3. Upper panel shows the plot of the emittance growth rates after 200 lattice periods for $\sigma_0 = 100^\circ$ in which the envelope instability is manifested following the $4\sigma = 360^\circ$ fourth-order particle resonance. Here, the unit of $\langle \hat{P}_\theta \rangle$ is mm-mrad. Lower panel shows the plot of envelope instability stop band for $\sigma_0 = 100^\circ$ of a KV beam, which indicates the B-mode and Q-mode instabilities. The stop bands of the emittance growth rates become narrower and shift to higher σ/σ_0 regions as $\langle \hat{P}_\theta \rangle$ increases.

stabilities after the fourth-order resonance is manifested within 50 periods as depicted in Fig. 2. Independent of $\langle \hat{P}_\theta \rangle$, the stop band of the envelope instability for a fixed σ_0 is defined as a function of only σ/σ_0 [5, 7]. For $\langle \hat{P}_\theta \rangle = 0$, the envelope instability of the perturbed beam is significant mainly within and near the stop band of the B-mode (breathing mode) instability under the periodic solenoid channel. The emittance growth rate is maximum near the lower bound of the B-mode stop band and sharply drops to 1 outside the boundary [18, 30].

In contrast, the beam mismatch generated by the fourth-order resonance is reduced for the spinning beams, which accordingly mitigates the excitation of the envelope instability. In the region of $\sigma/\sigma_0 \leq 0.82$ in Fig. 2 (left side of the cyan arrow), the fourth-order particle resonance is mitigated. The beam mismatch and emittance growth are not sufficiently strong to develop the envelope instability, even though the tune depression lies within the instability stop band. Therefore, the stop bands of the emittance growth rates in Fig. 3 shift to the right and become narrower as $\langle \hat{P}_\theta \rangle$ increases (see the cyan arrow). The maximum growth rate also decreases, and the corresponding tune depression shifts to the right at the

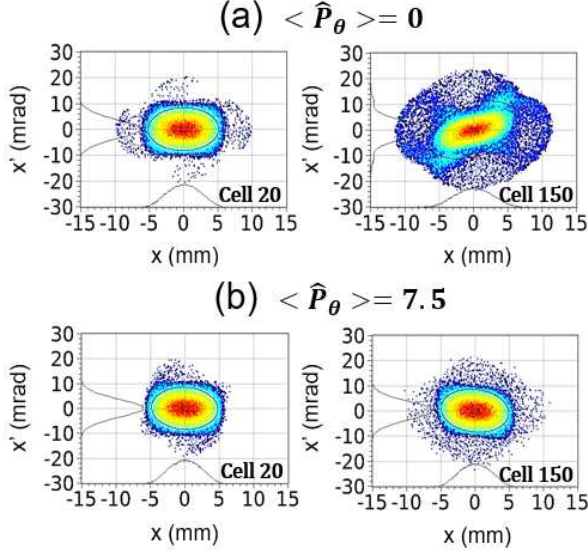


FIG. 4. Particle phase space plots for $\sigma_0 = 100^\circ$. For (a) $\langle \hat{P}_\theta \rangle = 0$ and $\sigma = 72^\circ$, the fourfold structure is dominantly observed, which eventually leads to a beam mismatch and B-mode instability. For (b) $\langle \hat{P}_\theta \rangle = 7.5$ mm-mrad and $\sigma = 72.5^\circ$, the fourth-order resonance is mitigated, and envelope instability is not induced even after 150 lattice periods. Emittance growth rates are (a) 1.04 and (b) 1.02 at cell 20, and (a) 2.27 and (b) 1.06 at cell 150, respectively.

same time. When the beam has a large average angular momentum in the range of $\sigma/\sigma_0 = 0.84 \sim 0.86$, the emittance growth rates in Fig. 3 are still considerable despite the lower growth rates compared with $\langle \hat{P}_\theta \rangle = 0$ case in the early stage (see Fig. 2). We note that there is a Q-mode (quadrupole mode) instability, and the beams are affected more by the Q-mode owing to the shifted stop bands in the low beam current region. As the beam current decreases further such that $\sigma/\sigma_0 > 0.9$, both the fourth-order particle resonance and envelope instability are not observed.

The detailed beam distributions in the $x - x'$ phase-space plane are plotted in Fig. 4. Figure 4(a) shows the projections of particles at lattice cells 20 and 150 when $\langle \hat{P}_\theta \rangle$ equals 0 and $\sigma = 72^\circ$. At cell 20, the resonance particles constitute the fourfold structure moving outwards from the center, where the emittance growth rate becomes approximately 1.04, as shown in Fig. 2. Eventually, the beam grows to the envelope instability at cell 150 because it is within the stop band. The corresponding emittance growth rate becomes approximately 2.27, as can be seen from Fig. 3. Figure 4(b) illustrates the projections of $\langle \hat{P}_\theta \rangle = 7.5$ mm-mrad beam when $\sigma = 72.5^\circ$. At cell 20, we clearly observe that the fourth-order particle resonance is mitigated with fewer particles populating the fourfold structure than Fig. 4(a). The beam particles gather close to the stable central region with a smaller emittance growth rate of 1.02. As a result, the envelope instability is not induced along 150 periods, and

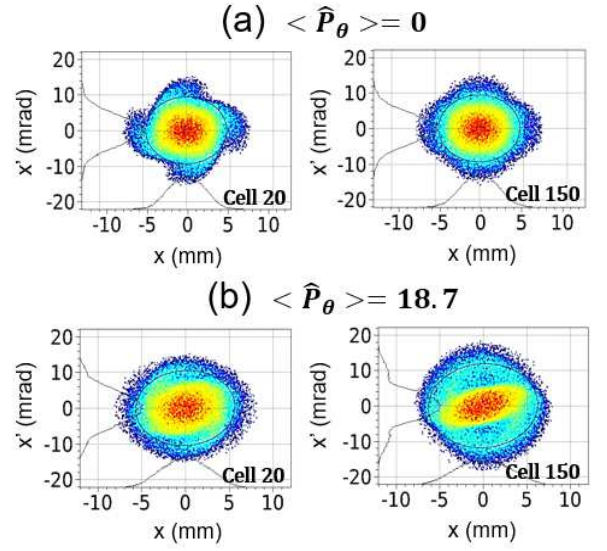


FIG. 5. Particle phase space plots for $\sigma_0 = 100^\circ$. For (a) $\langle \hat{P}_\theta \rangle = 0$ and $\sigma = 84^\circ$, the fourth-order resonance persists over 150 lattice periods. For (b) $\langle \hat{P}_\theta \rangle = 18.7$ mm-mrad and $\sigma = 86^\circ$, the fourth-order resonance is mitigated, but a Q-mode instability occurs after 150 lattice periods. Emittance growth rates are (a) 1.09 and (b) 1.02 at cell 20, and (a) 1.09 and (b) 1.45 at cell 150, respectively.

the emittance growth rate does not change considerably (only from 1.02 to 1.06).

Figure 5 shows the particle projections for the lower beam currents. The emittance growth rate in Fig. 5(a) is 1.09 at cell 20, and the fourfold structure can be more clearly observed than the spinning beam. Nevertheless, because $\sigma = 84^\circ$ is outside the stop band of the envelope instability, the fourth-order resonance persists over 150 periods and the emittance growth rate remains 1.09. For $\langle \hat{P}_\theta \rangle = 18.7$ mm-mrad beam in Fig. 5(b), the emittance growth rate is 1.02 at cell 20, and 1.45 at cell 150. As discussed previously, the large average angular momentum beams are affected more by the Q-mode instability for the tune depression of 0.86. Therefore, the emittance growth rate at cell 150 is larger than the case of $\langle \hat{P}_\theta \rangle = 0$, but is less fatal than the B-mode instability.

In summary, we have demonstrated beam spinning as a possible control knob for mitigating the fourth-order particle resonance and the subsequent envelope instability. Unlike the other approaches based on nonlinear lattices [20, 31], which may require complicated design and reconfiguration of the focusing elements, the proposed scheme can be readily applied to high-intensity linacs with periodic solenoidal channels. The technology for the beam spinning is based on several well-established experiments [22, 32, 33]. Using a thin carbon foil in the MEBT section of the Spallation Neutron Source (SNS), a previous study reported the stripping of 2.5 MeV H^- to proton beam with an efficiency of 99.98% and emittance growth of only 10–20% [32]. If we strip the H^-

beam inside a solenoid field B_z as in the emittance transfer experiment (EMTEX) [22], $\langle \hat{P}_\theta \rangle = 2\kappa_0\sigma_r^2$ with $\kappa_0 = \{[(B\rho)_{\text{in}}/(B\rho)_{\text{out}}] - 1\} [B_z/2(B\rho)_{\text{in}}]$, where $(B\rho)_{\text{in}}$ and $(B\rho)_{\text{out}}$ are the beam rigidity before and after the foil, respectively [33]. For a 2.5 MeV H^- beam with $\sigma_r = 2$ mm, we have $|\langle \hat{P}_\theta \rangle| \lesssim 35$ mm-mrad for $|B_z| \leq 1$ T. For a 2.5 MeV/u D^- beam with similar conditions, we expect an outgoing deuteron beam with $|\langle \hat{P}_\theta \rangle| \lesssim 12$ mm-mrad. Hence, the experimentally available ranges of $\langle \hat{P}_\theta \rangle$ would cover most of the simulation settings presented in this Letter.

Finally, it is worthwhile to mention an interesting analogy between spinning beams and flying objects such as American footballs, spinning rockets, and rifled bullets. Spinning flying objects are stabilized against small disturbances by maintaining a large angular momentum

vector in a specific direction [34]. In some situations, the spinning averages out a misaligned thrust to the object [34]. Motivated by this analogy, we plan to further investigate the possible benefits of beam spinning in dealing with machine imperfections and initial beam mismatches.

This work was supported by the National Research Foundation (NRF) of Korea (Grant Nos. NRF-2019R1A2C1004862 and NRF-2020R1A2C1010835). This work was also supported by the Rare Isotope Science Project of the Institute for Basic Science funded by the Ministry of Science and ICT (MSIT) and the NRF of Korea under Contract 2013M7A1A1075764.

*Authors to whom correspondence should be addressed: mchung@unist.ac.kr and jeond@ibs.re.kr

-
- [1] R. C. Davidson and H. Qin, *Physics of Intense Charged Particle Beams in High Energy Accelerators* (World Scientific, Singapore, 2001).
- [2] M. Reiser, *Theory and Design of Charged Particle Beams*, 2nd ed. (Wiley-VCH, Weinheim, 2008).
- [3] T. Wangler, *RF Linear Accelerators*, 2nd ed. (Wiley-VCH, Weinheim, 2008).
- [4] I. Hofmann, *Space Charge Physics for Particle Accelerators* (Springer, Switzerland, 2017).
- [5] I. Hofmann, *Part. Accel.* **13** (1982).
- [6] C. Chen and R. C. Davidson, *Phys. Rev. Lett.* **72**, 2195 (1994).
- [7] S. M. Lund and B. Bukh, *Phys. Rev. ST Accel. Beams* **7**, 024801 (2004).
- [8] C. Li and Q. Qin, *Phys. Plasmas* **22**, 023108 (2015).
- [9] J. Qiang, *Phys. Rev. ST Accel. Beams* **21**, 034201 (2018).
- [10] D. Jeon, J. A. Holmes, V. V. Danilov, J. D. Galambos, and D. K. Olsen, *Phys. Rev. E* **60**, 7479 (1999).
- [11] G. Franchetti, I. Hofmann, M. Giovannozzi, M. Martini, and E. Metral, *Phys. Rev. ST Accel. Beams* **6**, 124201 (2003).
- [12] D. Jeon, L. Groening, and G. Franchetti, *Phys. Rev. ST Accel. Beams* **12**, 054204 (2009).
- [13] L. Groening, W. Barth, W. Bayer, G. Clemente, L. Dahl, P. Forck, P. Gerhard, I. Hofmann, M. S. Kaiser, M. Maier, *et al.*, *Phys. Rev. Lett.* **102**, 234801 (2009).
- [14] Dong-O. Jeon, *Phys. Rev. Accel. Beams* **19**, 010101 (2016).
- [15] D. Jeon, J. Jang, and H. Jin, *Nucl. Instrum. Methods, sect. A* **832**, 43 (2016).
- [16] D. Jeon and K. R. Hwang, *Phys. Plasmas* **24**, 063108 (2017).
- [17] D.-O. Jeon, *J Korean Phys. Soc.* **72**, 1523 (2018).
- [18] Y. L. Cheon, S. H. Moon, M. Chung, and D. Jeon, *Phys. Plasmas* **27**, 063105 (2020).
- [19] V. Shiltsev, Y. Alexahin, A. Burov, and A. Valishev, *Phys. Rev. Lett.* **119**, 134802 (2017).
- [20] S. D. Webb, D. L. Bruhwiler, D. T. Abell, A. Sishlo, V. Danilov, S. Nagaitsev, A. Valishev, K. Danilov, and J. R. Cary, arXiv preprint arXiv:1205.7083 (2012).
- [21] C. Chen, R. Pakter, and R. C. Davidson, *Phys. Rev. Lett.* **79**, 225 (1997).
- [22] L. Groening, M. Maier, C. Xiao, L. Dahl, P. Gerhard, O. K. Kester, S. Mickat, H. Vormann, M. Vossberg, and M. Chung, *Phys. Rev. Lett.* **113**, 264802 (2014).
- [23] T. P. Wangler, K. R. Crandall, R. Ryne, and T. S. Wang, *Phys. Rev. ST Accel. Beams* **1**, 084201 (1998).
- [24] Q. Qian, R. C. Davidson, and C. Chen, *Phys. Plasmas* **2**, 2674 (1995).
- [25] R. L. Gluckstern, *Phys. Rev. Lett.* **73**, 1247 (1994).
- [26] Y.-E. Sun, P. Piot, K.-J. Kim, N. Barov, S. Lidia, J. Santucci, R. Tikhoplav, and J. Wennerberg, *Phys. Rev. ST Accel. Beams* **7**, 123501 (2004).
- [27] K.-J. Kim, *Phys. Rev. ST Accel. Beams* **6**, 104002 (2003).
- [28] D. Uriot and N. Pichoff, in *Proceedings of the 6th International Particle Accelerator Conference, Richmond, VA* (2015) p. 92.
- [29] L. Groening, C. Xiao, and M. Chung, *Phys. Rev. Accel. Beams* **21**, 014201 (2018).
- [30] I. Hofmann and O. Boine-Frankenheim, *Phys. Rev. Lett.* **115**, 204802 (2015).
- [31] Y. Batygin, A. Scheinker, S. Kurennoy, and c. Li, *Nucl. Instrum. Methods, sect. A* **816**, 78 (2016).
- [32] A. Shishlo, J. Galambos, A. Aleksandrov, V. Lebedev, and M. Plum, *Phys. Rev. Lett.* **108**, 114801 (2012).
- [33] M. Chung, H. Qin, R. C. Davidson, L. Groening, and C. Xiao, *Phys. Rev. Lett.* **117**, 224801 (2016).
- [34] R. D. Lorenz, *Spinning Flight: Dynamics of Frisbees, Boomerangs, Samaras, and Skipping Stones* (Springer, New York, 2006).